HIGH POWER LASER
SCIENCE AND ENGINEERING

RESEARCH ARTICLE

Interaction of a counter-propagating relativistic laser pair with subwavelength thin solid-density foil

Xiangrui Jiang [1,2], Debin Zou [1], Mingyang Yu[3], Kaiyuan Feng [1], Xiaohu Yang [2], Huanwen Chen [1], Lixiang Hu[1], Weiquan Wang[1], Guobo Zhang [2], Fuqiu Shao[1], Wenhui Tang[2], and Tongpu Yu [1]

[1] *Department of Physics, National University of Defense Technology, Changsha, China*

[2] *Department of Nuclear Science and Technology, National University of Defense Technology, Changsha, China*

[3] *College of Engineering Physics, Shenzhen Technology University, Shenzhen, China*

(Received 2 December 2024; revised 18 January 2025; accepted 10 February 2025)

Abstract

The effect of the polarizations of two counter-propagating relativistic laser pulses interacting with subwavelength thin solid-density foil is investigated. Three-dimensional particle-in-cell simulations and analytical modelling show that the interaction and resulting transverse instability depend strongly on the polarization directions as well as the intensity distribution of the resultant light field in the foil. The left- and right-handed circularly polarized laser pair with the same phase at the common focal spot in the ultrathin foil leads to the strongest distortion of the foil. The fastest growing mode and maximum growth rate depend mainly on the laser intensity. For all polarization and phase-difference combinations, the instability is weakest when the two laser pulses are exactly out of phase at the common focusing point in the foil.

Keywords: counter-propagating lasers; dynamics; thin foil; transverse instability

1. Introduction

The Rayleigh–Taylor instability (RTI)[1,2] is a well-studied hydrodynamic process. It has been found to play detrimental roles in inertial confinement fusion (ICF)[3–5] and laser-driven charged-particle accelerators[6–11]. In the past decade, there have been many efforts to clarify the differences and contributions of the mechanisms in the development of the RTI-like[11–15] and Weibel-like[16] instabilities found in laser–matter interactions. In particular, Wan *et al.*[17] showed that the coupling of electrons and ions plays an important role in the transverse instability of laser-driven thin foils. Chou *et al.*[14,15] found that the onset of strong electron heating is related to laser-driven RTI.

Relativistic, especially counter-propagating, laser pulses interacting with thin foils have been suggested for producing intense few-cycle terahertz radiation[18–21], dense electron–positron pairs and γ-rays[22,23], as well as neutron bunches[24–27]. Such interactions are also of great basic physics interest since subwavelength thin foils can serve as medium for coupling intense short laser pulses without first significantly alternating their properties. However, the existing works are mainly one- or two-dimensional (1D or 2D), so the effects associated with the third dimension remain unclear.

In this paper, we investigate the dynamics and stability of two counter-propagating relativistic laser pulses interacting in a subwavelength thin solid-density foil by three-dimensional (3D) particle-in-cell (PIC) simulation and analytical modelling. For the left- and right-handed circularly polarized (LCP and RCP) incident laser pair, we found that a grainy bubble-and-rings density structure similar to that found in RTI due to radiation-pressure acceleration (RPA) appears on the foil plane. The criteria, growth rates and properties of the unstable structure depend strongly on the polarization, phase and magnitude of the resultant laser field in the ultrathin foil, and the instability is weakest if the two lasers are exactly out of phase. Our result suggests that one can perhaps control instabilities in thin foils with properly tailored laser pulse(s).

Section 2 gives the parameters of the lasers and ultrathin foil in our simulations. Section 3 investigates the evolution of the foil plasma and the laser lights. Section 4 presents an analytical model for the laser–foil interaction, especially the evolution of the polarization and intensity distribution of the resultant laser light. In Section 5, the conditions and properties, as well as their dependence on the laser intensity and phase, of the instabilities are discussed in terms of a

Correspondence to: D. B. Zou, Department of Physics, National University of Defense Technology, Changsha 410073, China. Email: debin-zou@nudt.edu.cn

1

relativistic two-fluid model. Section 6 presents additional discussion of the results. A summary is given in Section 7.

2. Laser and target parameters

We carried out 3D simulations with the PIC code EPOCH[28] to investigate the interaction of two counter-propagating relativistic laser pulses incident on a subwavelength thin foil and the resulting foil evolution. The simulation box size is $x \times y \times z = 20\lambda_0 \times 20\lambda_0 \times 20\lambda_0$, with $800 \times 400 \times 400$ cells, where $\lambda_0 = 1$ μm is the laser wavelength. Each cell contains 27 electrons and 27 ions. Open boundary conditions are used for both the fields and particles. Thanks to rapid ionization by the laser prepulse, the thin foil is modelled by a fully ionized cold hydrogen plasma layer located at $-0.05\lambda_0 < x < 0.05\lambda_0$ and $-10\lambda_0 < y < 10\lambda_0$. The plasma density is $n_e = n_p = 50n_c$, where $n_c = m_e\omega_0^2\varepsilon_0/e^2$ is the critical density, ω_0 is the laser frequency, ε_0 is the permittivity in vacuum and $-e$ and m_e are the electron charge and rest mass, respectively. The two identical laser pulses propagate along the $\pm x$-directions and are focused at the centre of the $0.1\lambda_0$-thin foil. The space–time profile of the lasers is $a_0 \exp[-(r/r_0)^2]\sin^2(\pi t/2\tau_0)$, where $r_0 = 5\lambda_0$

is the focal spot radius, $\tau_0 = 10T_0$ is the pulse duration, $T_0 = 3.3$ fs is the laser period and $a_0 = eE_0/m_e\omega_0c = 20$ is the normalized laser amplitude. Here, E_0 is the peak laser electric field and c is the speed of light in vacuum. That is, the intensity, power and energy of each laser are $I_0 = 5.5 \times 10^{20}$ W/cm^2, 215 TW and 5.4 J, respectively.

We shall consider linearly polarized (LP) and circularly polarized (CP) laser pairs. As some laser pairings are physically identical in the interactions, we shall concentrate only on the pairs yLP + yLP, yLP + zLP, LCP + LCP and LCP + RCP for phase differences $\Delta\varphi = 0, \pi/2, \pi$ and $3\pi/2$ between the paired lasers, that is, there are 16 distinct cases. For clarity, here yLP and zLP, and LCP and RCP denote y- and z-direction LP lasers, and the left- and right-handed CP lasers, respectively, and the $+$ sign denotes pairing. Moreover, unless otherwise stated, foil- or ion-density distribution shall refer to that on the foil plane.

3. Dynamics of two counter-propagating lasers interacting with ultrathin foil

The left-hand panel of Figure 1 shows the evolution of the side (x, y) and foil-plane (z, y) distributions of the foil, or
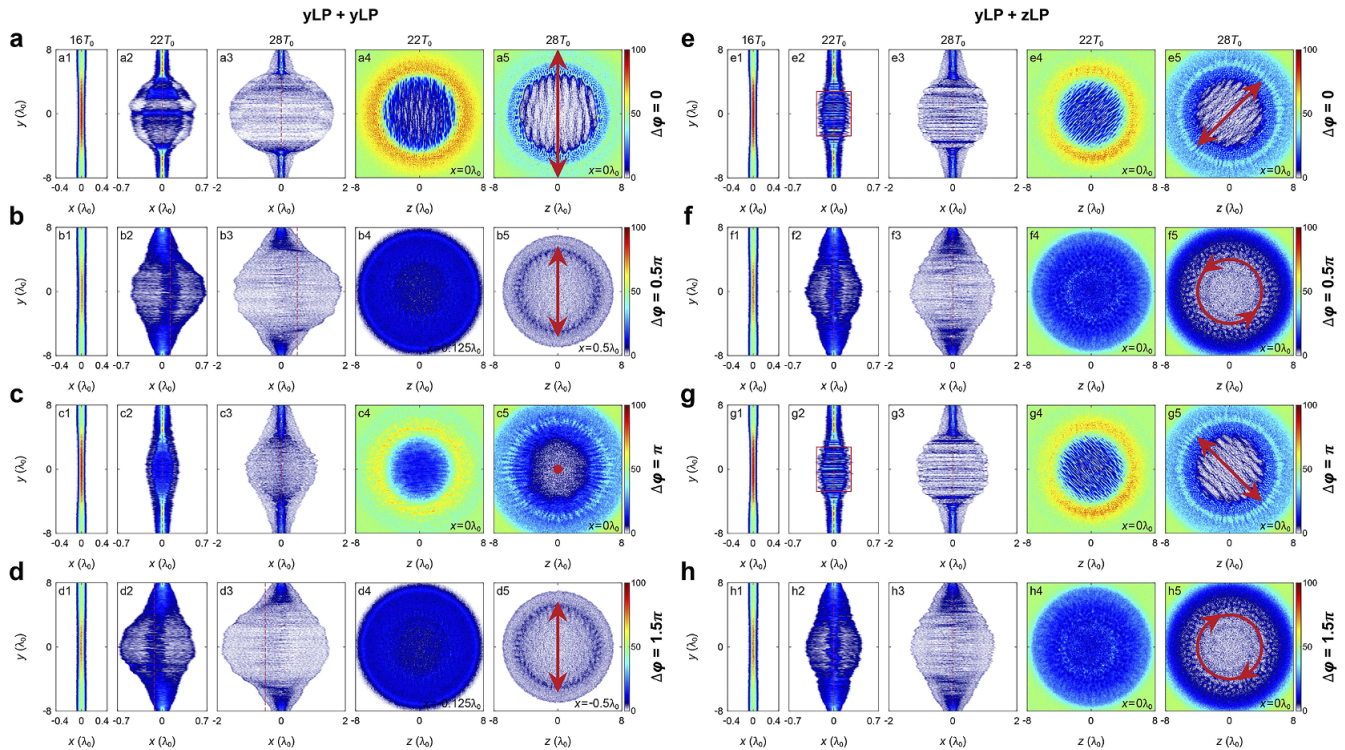

Figure 1. Evolution of the foil density for different polarizations of the laser pair: (a)–(d) yLP and yLP and (e)–(h) yLP and zLP, with (a) and (e) $\Delta\varphi = 0$, (b) and (f) $\pi/2$, (c) and (g) π, and (d) and (h) $3\pi/2$. Here, yLP and zLP denote linear polarization in the y- and z-directions, respectively, and $\Delta\varphi$ is the phase difference between the two lasers. The first three columns of both the yLP (left-hand panel) and zLP (right-hand panel) cases show the axial (with respect to the lasers) foil-density distribution in the $z = 0$ plane at $t = 16T_0$, $22T_0$ and $28T_0$, respectively. The fourth and fifth columns in both the left- and right-hand panels show the transverse density distributions at the axial locations defined by the vertical dashed red lines in the second and third columns (for $t = 22T_0$ and $28T_0$), respectively. In all panels, the red lines/curves with arrows show the amplitude and displacement direction of the analytically obtained resultant electric field (shown in Table 1) of the two colliding lasers at $x = 0$, where the subscript 'r' here denotes 'resultant'. The large red centre dot in window (c5) corresponds to $E_r = 0$, that is, the fields of the two lasers cancelled each other out.
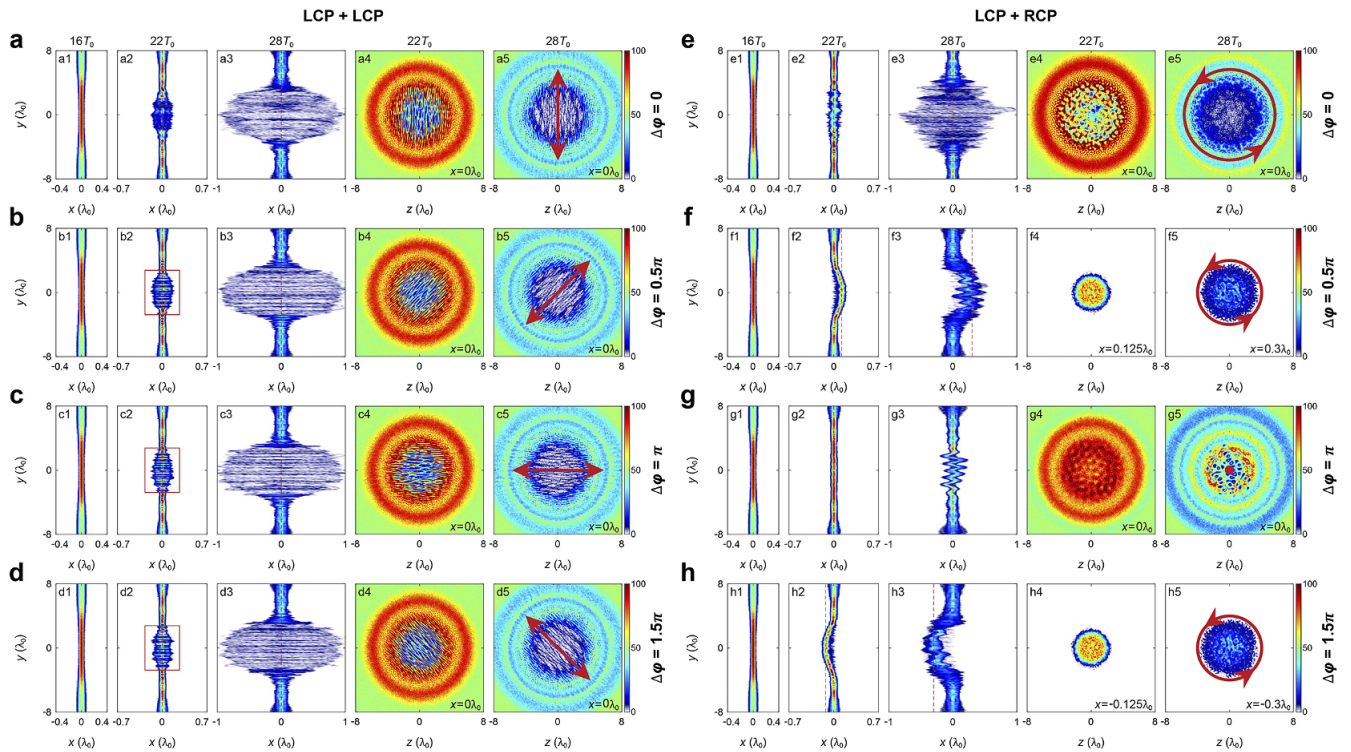
Figure 2. Evolution of the foil-density distribution for the polarization combinations (a)–(d) LCP + LCP and (e)–(h) LCP + RCP with (a) and (e) $\Delta\varphi = 0$, (b) and (f) $\pi/2$, (c) and (g) π, and (d) and (h) $3\pi/2$. The first to third columns show the longitudinal foil-density distribution in the $z = 0$ plane at $t = 16T_0$, $22T_0$ and $28T_0$, respectively. The fourth and fifth columns show the transverse ion distribution in the planes indicated by the red dashed lines in the second and third columns at $t = 22T_0$ and $28T_0$, respectively. The red lines and arrows in the fifth column represent the magnitude and direction of the resultant radial electric field at $x = 0$. The dot in panel (g5) indicates $E_r = 0$.

ion, density for yLP + yLP laser pair interaction with the foil for different $\Delta\varphi$ values. One can see that the foil is first locally compressed by the focusing lasers. Then, for $\Delta\varphi = 0$ and π (Figures 1(a) and 1(c)), the compressed foil centre region begins to expand to the left and right symmetrically. The expansion for $\Delta\varphi = \pi$ is weaker since the lasers are out of phase, so that cancellation of their fields occurs. For $\Delta\varphi = \pi/2$ $(3\pi/2)$, the laser pulse from the left (right) has a quarter-period phase lead (lag), so that the affected plasma is pushed to the right (left) by the net light pressure[21]. Of interest is that for $\Delta\varphi = 0$, filament-like streaks along y appear in the foil-density distribution, but for $\Delta\varphi = \pi/2$, π and $3\pi/2$ the density is azimuthally symmetric. The right-hand panel for the yLP + zLP pair shows that the foil density is always left–right symmetric. For $\Delta\varphi = 0$ and π, streaks along x (such as that marked by the red box in the Figure 1(g2)) appear. The transverse features for $\Delta\varphi = 0$ and π are similar, except that the streaks are oriented along the $y = z$ direction for $\Delta\varphi = 0$ and along the $y = -z$ direction for $\Delta\varphi = \pi$. In both cases, the distribution of the high-density region is identical. This is because the laser intensity is lower outside the laser focal spot and the foil is opaque and will be compressed by the laser ponderomotive force, rather than being modulated by the transmitted overlap laser field in the central region of the foil. For $\Delta\varphi = \pi/2$ and $3\pi/2$, Figures 1(f4), 1(f5), 1(h4) and 1(h5) show that the density

distribution has an annular ring and grainy bubble structure, which has also been observed in light-sail experiments[11] and simulations[17].

Next we consider counter-propagating CP laser pairs LCP + LCP and LCP + RCP. Figure 2 shows that the foil expands more slowly than that of the yLP + yLP and yLP + zLP pairs, which is expected since the pressure of CP light has only a non-oscillating component. For the LCP + LCP pair, we see in the left-hand panel that the side-view of the foil density is left–right symmetric for all values, and Figures 2(b2), 2(c2) and 2(d2) have similar features to those in Figures 1(e2) and 1(g2). Streaks similar to those in Figures 1(e5) and 1(g5) also appear, and their directions are also $\Delta\varphi$ dependent. The second column of the right-hand panel in Figure 2 shows that for the LCP + RCP pair the foil centre is more tightly compressed. For $\Delta\varphi = 0$ and π (first and third rows), the density remains symmetric, but it is more rapidly destroyed for $\Delta\varphi = 0$ than that for $\Delta\varphi = \pi$. For $\Delta\varphi = \pi/2$ and $3\pi/2$ (second and fourth rows), the foil centre is pushed to the right and left, respectively, as in the corresponding cases for LP laser pairs. Moreover, in all the cases here, the centre of the foil is rather heavily distorted. The fourth and fifth columns show that the foil density in the transverse direction has a grainy bubble centre and periodic less grainy annular rings outside. The above results show that the affected foil region can expand, be driven forward

or backward and form streaks and grainy bubbles and rings. In the following, we shall investigate these features in more detail.

4. Model for the laser interaction in the foil

As the solid-density foil is only $0.1\lambda_0$ thin, it is effectively transparent to the incident laser pulses[29]. We first assume that it is fully transparent with reflection ratio $R = 0$ to obtain a simple analytical solution of the intensity distribution of the resultant laser field. Since we are interested in the interaction time of less than one laser period, the electric fields of the yLP + yLP laser pair can be represented by the plane electromagnetic (EM) waves:

$$\begin{cases} E_{y,L} = E_0 \cos(\omega_0 t - k_0 x), \\ E_{y,R} = E_0 \cos(\omega_0 t + k_0 x + \Delta\varphi), \end{cases} \quad (1)$$

where $k_0 = \omega_0/c$ is the wave number, $t = 0$ is the time when the peaks of the lasers meet at the foil centre and the subscripts L and R denote being from the left and the right. For simplicity, hereafter the time and space quantities are normalized by ω_0^{-1} and k_0^{-1}, respectively. The resultant electric field of the two yLP lasers is then as follows:

$$\begin{aligned} E_y &= E_{y,L} + E_{y,R} \\ &= 2E_0 \cos(t + \Delta\varphi/2) \cos(x + \Delta\varphi/2). \end{aligned} \quad (2)$$

Since any CP EM wave propagating in the x-direction can be represented by two LP waves polarized in the y- and z-directions, the CP laser pair LCP + LCP can be represented by the following:

$$\begin{cases} E_{y,L} = E_0/\sqrt{2} \cos(t - x), \\ E_{z,L} = -E_0/\sqrt{2} \sin(t - x), \\ E_{y,R} = E_0/\sqrt{2} \cos(t + x + \Delta\varphi), \\ E_{z,R} = E_0/\sqrt{2} \sin(t + x + \Delta\varphi). \end{cases} \quad (3)$$

The resultant electric field for the LCP + LCP case is thus as follows:

$$\begin{cases} E_y = \sqrt{2}E_0 \cos(t + \Delta\varphi/2) \cos(x + \Delta\varphi/2), \\ E_z = \sqrt{2}E_0 \cos(t + \Delta\varphi/2) \sin(x + \Delta\varphi/2). \end{cases} \quad (4)$$

Similarly, the resultant fields of the other pairs can be obtained.

The results for the four laser pairs of interest from the analysis above are summarized in Table 1, and the corresponding simulation results are already shown by the (if any) solid red lines, curves, arrows and dots in the fifth columns of both the left- and right-hand panels of Figures 1 and 2. For example, if the resultant field is LP, the foil-density distribution has a streak pattern, whose direction is the same as that of the polarization from the theory. For the yLP + yLP case with $\Delta\varphi = \pi/2 \ (3\pi/2)$, the streaks disappear thanks to the right-hand (left-hand) foil displacement, and for $\Delta\varphi = \pi$, the density distribution is azimuthally symmetric (since $E_r = 0$). When the resultant field is CP, the density is annularly symmetric, also in agreement with the simple theory (as well as from experiments[11], as mentioned above).

Next we consider the origins of the different foil-density profiles. From the second and fifth columns in Figures 1 and 2, one can see that the filamentous streaks structure (marked by the red boxes) along the x-direction exists only if the resultant laser field is LP and polarized in the z-direction. The oscillating component of the light pressure force of the resultant LP laser light drives directed periodic perturbations that lead to density striation. Strictly speaking, the foil centre can only be smoothly pushed to the left or right by the net light pressure of two laser pulses. The steady-state model of Shen and Meyer-ter-Vehn[21] shows that the foil motion is determined by the net light pressure $\Delta P = P_{\text{left}} - P_{\text{right}}$ on the foil that is related to $\Delta\varphi$, where P_{left} and P_{right} are the light pressure on the left- and right-hand surfaces of the foil, respectively. However, this model is limited to continuously incident CP lasers and 1D geometry, and there are only stationary analytical solutions for two lasers with the same rotation direction. In addition, transverse instabilities are excluded. Here, we present a more general analysis of our results. Note that even though the foil is relativistically transparent, it cannot be ignored, that is, the reflection coefficient $R > 0$ and the transmission coefficient $T < 1$. Since the resultant electric field is nonuniform longitudinally, there is a pressure difference ΔP. For the case yLP + yLP, the normalized intensity of the y-component E_y^2/E_0^2 of the resultant laser light along the x-direction at $t = 0$ is given in Figure 3(a) for different $\Delta\varphi$ values. The direction of ΔP is determined by the slope $k|_{x=0} = \partial_x E_y^2|_{x=0}$, where k also represents the difference in the momentum flow of the EM field between the left- and right-hand laser pulses since the EM momentum $|\vec{g}|$ scales as E_y^2 ($|\vec{g}| = |\vec{E} \times \vec{B}|/\mu_0 =$

Table 1. The resultant electric field of two counter-propagating laser pulses.

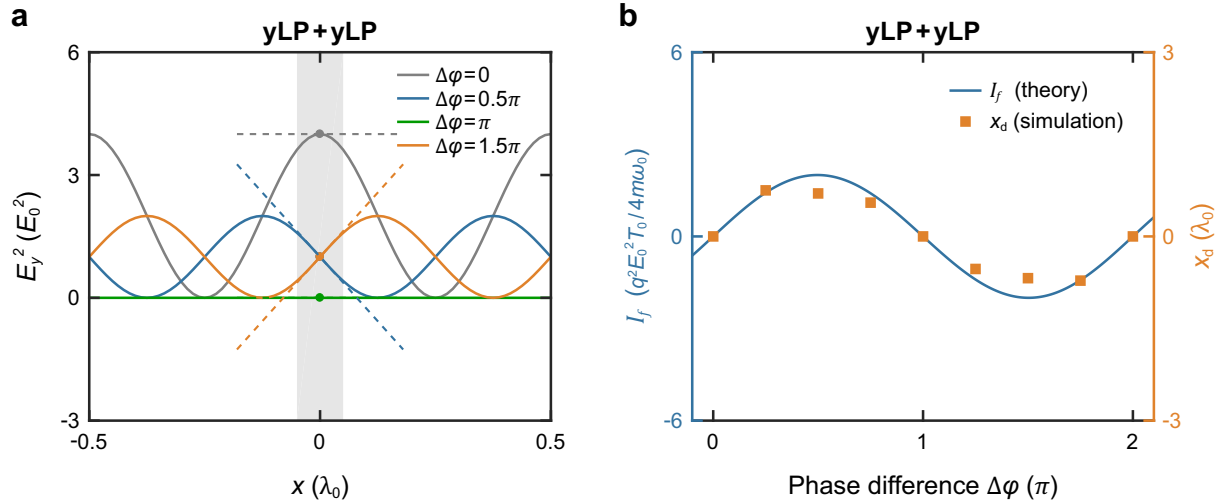|	E_y	E_z
yLP+yLP	$2E_0 \cos(t + \Delta\varphi/2) \cos(x + \Delta\varphi/2)$	0
yLP+zLP	$E_0 \cos(t - x)$	$E_0 \cos(t + x + \Delta\varphi)$
LCP+LCP	$\sqrt{2}E_0 \cos(t + \Delta\varphi/2) \cos(x + \Delta\varphi/2)$	$\sqrt{2}E_0 \cos(t + \Delta\varphi/2) \sin(x + \Delta\varphi/2)$
LCP+RCP	$\sqrt{2}E_0 \cos(t + \Delta\varphi/2) \cos(x + \Delta\varphi/2)$	$-\sqrt{2}E_0 \sin(t + \Delta\varphi/2) \cos(x + \Delta\varphi/2)$

Figure 3. Results of the analytical model and PIC simulations. (a) Normalized intensity of the y component E_y^2/E_0^2 of the resultant laser field for the yLP + yLP case at $t = 0$. The shaded region represents the foil and the dashed lines represent the slopes of E_y^2 at $x = 0$. (b) The impulse I_f of the axial pressure force f_p (blue curve) of the resultant laser light in one laser cycle and the displacement x_d (orange squares) of the foil centre versus $\Delta\varphi$ for the yLP + yLP case.

$E^2/2\mu_0 c$, where μ_0 is the permeability in vacuum). We see that for $\Delta\varphi = 0$ and π, $k|_{x=0} = 0$ and thus $\Delta P = 0$, resulting in the longitudinally symmetrical compression of the foil, as shown in Figures 1(a) and 1(c). However, when $\Delta\varphi = \pi/2$ and $3\pi/2$, $k < 0$ and $k > 0$, corresponding to the cases of $\Delta P > 0$ and $\Delta P < 0$, respectively. The foil will be pushed to the right and left, respectively, which is in good agreement with Figures 1(b) and 1(d). In fact, $k = \partial_x E_y^2$ is consistent with the axial ponderomotive force $f_p = -\left(q^2/4m\omega_0^2\right)\partial_x E^2$ of the laser. Since the axial displacement of the foil is the result of continuous action of f_p, the impulse after integration over a laser period

$$I_f = \int_0^{T_0} f_p \mathrm{d}t = -\frac{q^2}{4m\omega_0^2}\int_0^{T_0}\frac{\partial E^2}{\partial x}\mathrm{d}t \qquad (5)$$

should be of interest. Figure 3(b) shows I_f versus the maximum foil displacement x_d at $t = 22T_0$ from the PIC simulations of the yLP + yLP case. We see that these relations are consistent with the discussions above; in particular, the axial displacement of the foil centre depends mainly on the impulse exerted by the resultant laser light on the foil.

Figure 4 shows the evolution of f_p and the relation between f_p and $\Delta\varphi$ for different polarization combinations. Here, $f_{py} = -\left(q^2/4m\omega_0^2\right)\partial_x E_y^2$ and $f_{pz} = -\left(q^2/4m\omega_0^2\right)\partial_x E_z^2$ are also given. For the yLP + yLP and yLP + zLP cases, Figures 4(a) and 4(b) show that f_p oscillates periodically with time. The difference between them is that for the yLP + yLP pair, f_p is either greater than or less than 0 (also seen in Figure 4(e)), so the foil may be pushed right or left. For the yLP + zLP case, f_p can be positive or negative, but its integral over one laser period is equal to 0 (i.e., $I_f = 0$), as shown in Figure 4(b). This results in a longitudinally symmetric distribution of foil density at different $\Delta\varphi$ values. When the two lasers

are CP, the superposition of f_{py} and f_{pz} (i.e., f_p) is constant for each $\Delta\varphi$, as seen in Figures 4(c) and 4(d). In the LCP + LCP case, $f_p \equiv 0$ (seen in Figures 4(c) and 4(g)) and the foil density is symmetrically distributed. Since there is no oscillating term in f_p, the expansion is slower than that due to the LP laser pair. For the LCP + RCP case, the relationship between f_p and $\Delta\varphi$ is fixed, as shown in Figure 4(h). When $\Delta\varphi$ is not an integral multiple of π, such as $\pi/2$ and $3\pi/2$, $f_p \neq 0$ and the foil is pushed longitudinally to one side, as shown in Figures 2(f) and 2(h). It should be mentioned that despite the simplicity of the above model, for the LCP + RCP polarization combination, both the relations between f_p (or I_f) and $\Delta\varphi$, t and the longitudinal motion of the thin foil are consistent with the 1D steady-state model of Shen and Meyer-ter-Vehn[21]. Moreover, the model is also suitable for other polarization combinations.

5. Transverse instability in foil driven by two counter-propagating laser pulses

We now consider the development of the transverse instability in the foil. The intensity of the 2D Fourier spectrum of the averaged transverse foil density may be used to track the evolution of the instability[17]. As examples, we first consider the LCP + LCP case for $\Delta\varphi = \pi/2$ and the LCP + RCP case for $\Delta\varphi = 0$, since their resultant fields are LP and CP, respectively. Figures 5(a) and 5(c) show the transverse distributions of the averaged density in these cases, and their Fourier spectra are given in Figures 5(b) and 5(d), respectively. We see that for the LCP + LCP case with $\Delta\varphi = \pi/2$, the dominant mode in the k space is $k_y = k_z$, consistent with the result that the direction of the streaks is the same as that of the polarization of the resultant laser field. For the yLP + yLP and yLP + zLP cases, except for those in
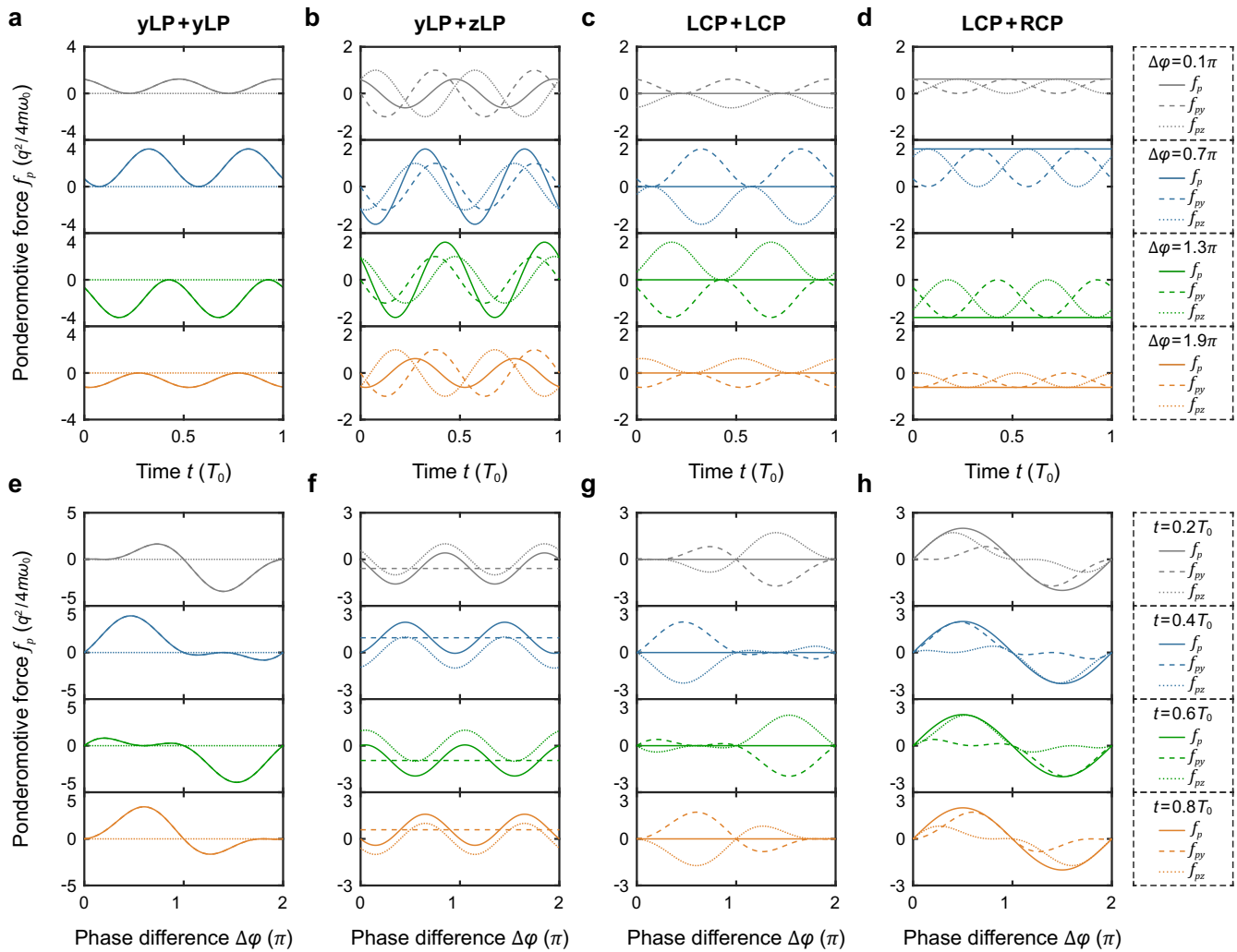
Figure 4. (a)–(d) Evolution of the light pressure force f_p in the axial (x) direction (solid curves) and (e)–(h) f_p versus $\Delta\varphi$ for different polarization combinations. In all cases, the transverse force components f_{py} (dashed curves) and f_{pz} (dotted curves) are also given.

Figures 1(c), 1(f) and 1(h), we can draw the same conclusion since the resultant laser fields are LP. It should be noted that this analysis of the very initial evolution of the foil with respect to the incident lasers does not identify the instability leading to foil destruction. In fact, the foil response to the resultant laser field is similar to that driven by a single LP laser. On the other hand, if the resultant field is CP, foil destruction can result from the transverse instability[11,17]. As shown in the right-hand panel of Figure 2 for the LCP + RCP case, a grainy bubble structure similar to that observed in the RPA light-sail experiments appears. Figures 5(c) and 5(d) show that the foil density is strongly modulated and the unstable mode has annular spatial distribution. The amplitude of the ring at $k_r = \left(k_y^2 + k_z^2\right)^{1/2}$ (grey circles in Figure 5(d)) then gives the relative magnitude of mode k, as shown in Figure 5(e). For the LCP + RCP case with $\Delta\varphi = 0$, the fastest growing mode and the maximum growth rate of the instability are $k_m = 2k_0$ and $\gamma_m = 0.98T_0^{-1}$, respectively. Note that although bubble structures also appear in Figures

1(f) and 1(h), they are located on the periphery of the laser affected area, and the foil expansion is similar to that of the LP laser pairs. Thus, in the following we shall mainly consider the instability of the LCP + RCP case.

Figure 6 shows the evolution of the fastest growing mode of the transverse instabilities in all the 16 cases. As shown in Figures 6(a)–6(d), the instability grows rapidly, then more slowly and the foil is eventually broken. The maximum growth rates γ_m are shown in Figure 6(e). For the yLP + yLP case, γ_m is positively correlated with E_r, as depicted by the lengths of the red arrows in the fifth column of the left-hand panel of Figure 1. For $\Delta\varphi = 0$ and π, γ_m is maximum and minimum, respectively. For $\Delta\varphi = 0$ and π of the yLP + zLP case, and for all $\Delta\varphi$ values of the LCP + LCP case (as shown in the fifth column of the right-hand panel of Figure 1 and the fifth column in the left-hand panel of Figure 2), γ_m remains roughly the same since E_r is similar in these cases. However, for the yLP + zLP case with $\Delta\varphi = \pi/2$ and $3\pi/2$, γ_m is somewhat smaller and E_r is also smaller, as depicted
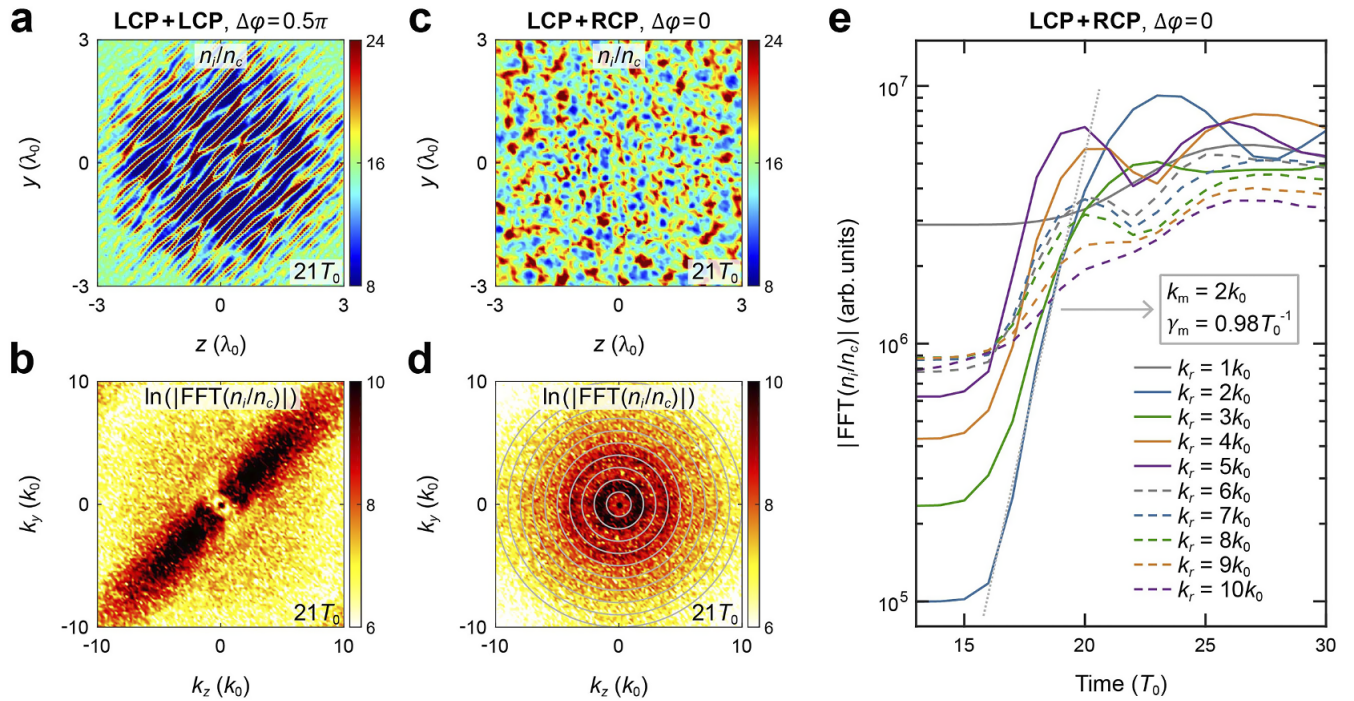
Figure 5. Averaged distribution of the foil density at $t = 21T_0$ for the (a) LCP + LCP case with $\Delta\varphi = \pi/2$ and (c) LCP + RCP case with $\Delta\varphi = 0$. (b), (d) 2D Fourier transform of the density distribution in (a) and (c), respectively. (e) Evolution of transverse instability of the LCP + RCP case for $\Delta\varphi = 0$ and different k_r values. The slope (dotted lines) of the fastest growing mode k_m shows the maximum growth rate γ_m.
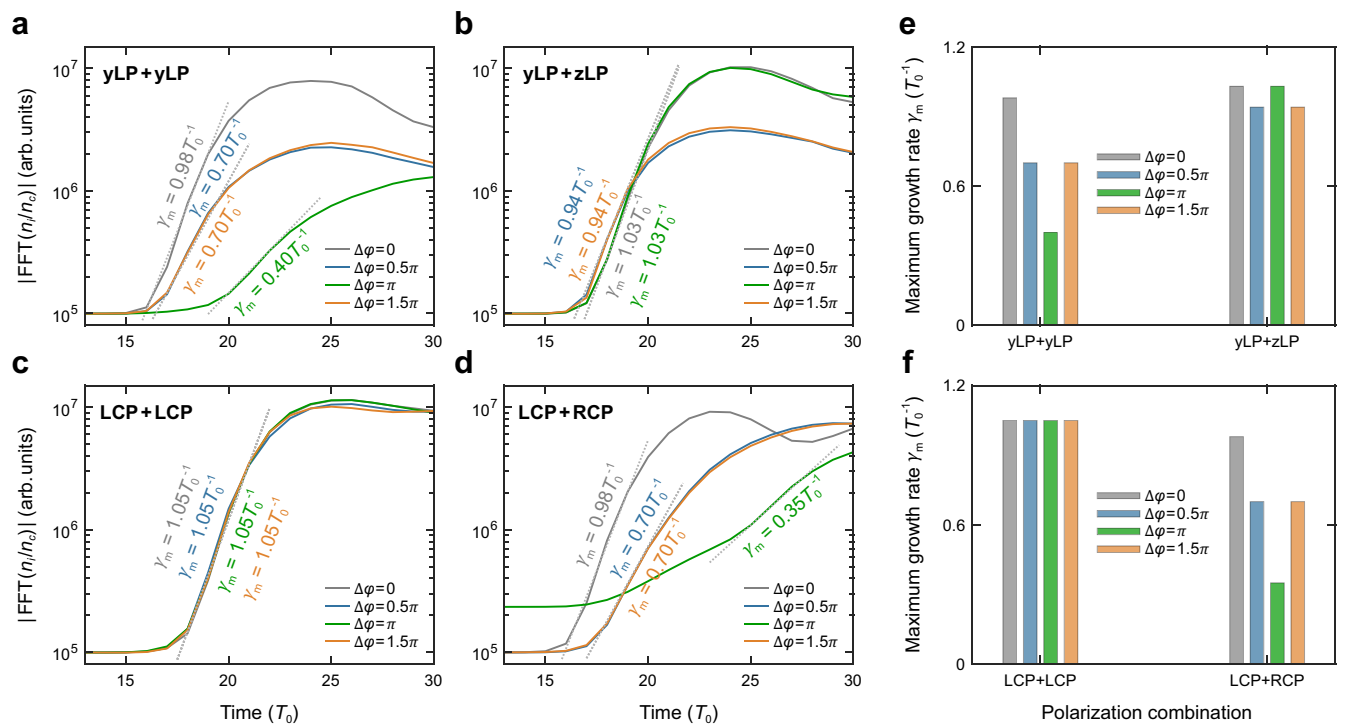

Figure 6. (a)–(d) Evolution of the fastest growing mode of transverse instability for all 16 cases. Here, the maximum growth rate γ_m (i.e., the slope) is labelled in (a)–(d). To compare intuitively, γ_m is also shown by a histogram, as seen in (e) and (f).
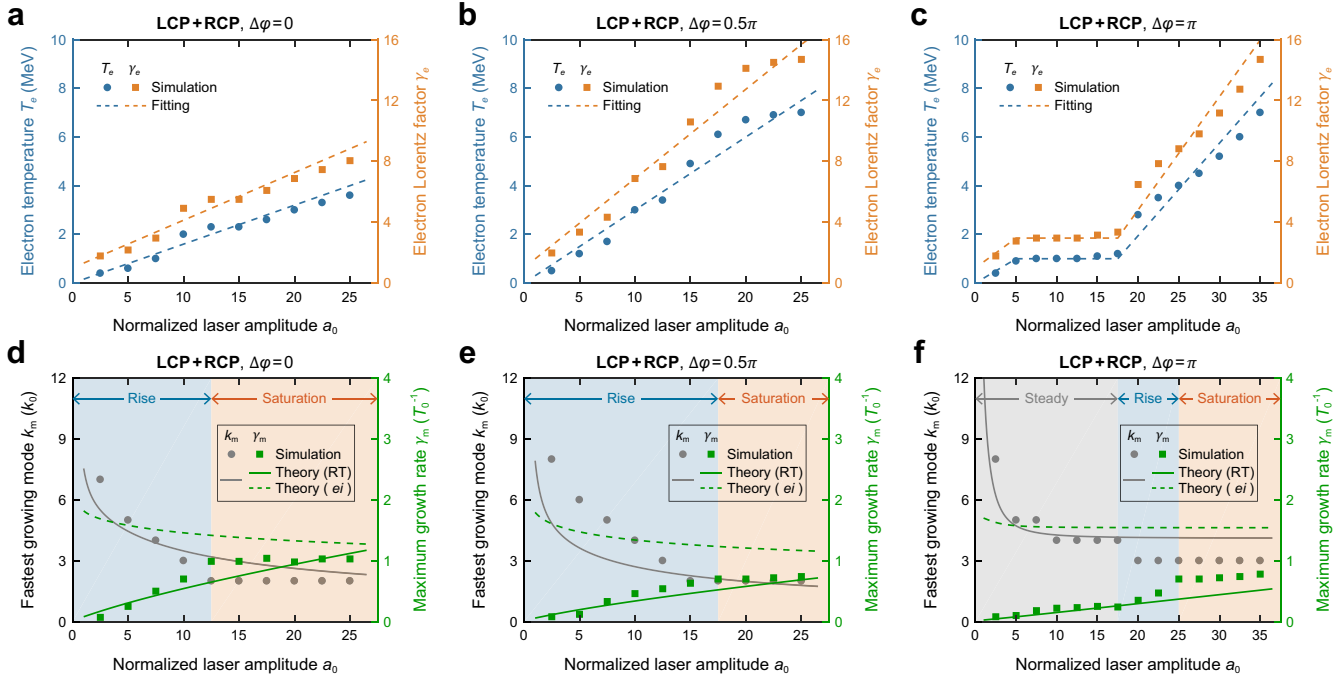
Figure 7. (a)–(c) Scaling laws of the electron temperature T_e (left-hand y-axis, blue dots) and Lorentz factor γ_e (right-hand y-axis, orange squares) versus a_0 for the LCP + RCP case with (a) $\Delta\varphi = 0$, (b) $\pi/2$ and (c) π from PIC simulations. The straight dashed lines are linear fits of the simulation results. (d)–(f) The fastest growing mode k_m (left-hand y-axis, grey dots) and maximum growth rate γ_m (right-hand y-axis, green squares) of transverse instability versus laser amplitude a_0 from PIC simulations for the LCP + RCP case with (d) $\Delta\varphi = 0$, (e) $\pi/2$ and (f) π. For comparison, the theoretical results from Equation (6) are also given: a solid green curve for RTI and a dashed green curve for the electron-ion (ei) coupling effect, and the grey curve for k_m is from Equation (7).

by the arrow lengths and circle diameters in the fifth column of the right-hand panel in Figure 1. Similar behaviour can be found in the LCP + RCP case, as shown in the fifth column of the right-hand panel of Figure 2. In fact, the fifth columns of the right-hand panel of Figure 2 and the left-hand panel of Figure 1 for the LCP + RCP and yLP + yLP cases, respectively, indicate that the dependence of γ_m and E_r on $\Delta\varphi$ is similar. For all 16 cases, γ_m is smallest if the laser pair is out of phase, or $\Delta\varphi = \pi$. As a result, the instability also develops slowest and the foil can thus be most tightly compressed.

The characteristics of the foil instability can be estimated from the 3D relativistic two-fluid theory of Wan et al.[17]. In the linear stage, the maximum growth rate is as follows:

$$\begin{cases} \gamma_{m,\mathrm{RT}} \simeq \left(\sqrt{\kappa/2}\,\alpha_{in}\omega_{pe}/v_{osc}\right)^{1/2}, \\ \gamma_{m,ei} \simeq 2\left(\omega_{pi}^2\omega_{pe}\right)^{1/3}(\kappa m_e/m_i)^{1/6}, \end{cases} \quad (6)$$

where $\kappa = (2c^2 - v_{osc}^2)/2\gamma_e c^2$, $v_{osc} = eE_0/\gamma_0 m_e \omega_0$ is the electron quiver velocity in the resultant field, $\gamma_e = T_e/m_e c^2 + 1$ is the Lorentz factor of the electrons, T_e is the electron temperature, $\gamma_0 = \left(1 + a_0^2/2\right)^{1/2}$ for LP and $\gamma_0 = \left(1 + a_0^2\right)^{1/2}$ for CP light, $\alpha_{in} = P_0/m_i n_e d_0$ is the axial ion speed, $P_0 = (1 + R - T)I_0/c$ is the light pressure, m_i is the ion mass and $\omega_{pe} = \left(e^2 n_e/\varepsilon_0 m_e\right)^{1/2}$ and $\omega_{pi} = \left(e^2 n_i/\varepsilon_0 m_i\right)^{1/2}$ are the

electron and ion plasma frequencies, respectively. According to the model of relativistic-induced transparency (RIT)[29], $R = \epsilon_0^2/a_0^2$ and $T = 1 - \epsilon_0^2/a_0^2$ when $a_0 > \epsilon_0 > 1$, where $\epsilon_0 = \omega_{pe}^2 d_0/2\omega_0 c$ characterizes the optical properties of the subwavelength foil. The wave number of the fastest growing mode of transverse instability is given by the following:

$$k_m = \sqrt{2\kappa}\,\omega_{pe}/v_{osc}. \quad (7)$$

The above analysis is for a single laser beam. To extend it to the interaction of a counter-propagating laser pair with a thin foil, it is necessary to replace P_0 with the combined pressure ΔP. Since the foil is nearly transparent to the incident light, the two lasers effectively merge into a resultant light bunch and the interaction of the two lasers with the foil can be approximated by that between the resultant light field and the thin foil. Since $x_d < \lambda_0$ (see Figures 2(f3) and 2(h3)), E_0, a_0 and I_0 can be replaced by those of the resultant laser field. Thus, k_m and γ_m for given laser and plasma parameters can be obtained.

Considering that the bubble structure in the LCP + RCP case is similar to that observed in the RPA experiments and simulations[11,17], we use this case as an example for analysing the transverse instability in more detail. Figures 7(a)–7(c) show the electron temperature T_e and γ_e versus a_0 for $\Delta\varphi = 0$, $\pi/2$ and π. The results for $\Delta\varphi = 3\pi/2$ are exactly the same as those of $\Delta\varphi = \pi/2$. We can see

that T_e and γ_e grow linearly with a_0 for both $\Delta\varphi = 0$ and $\pi/2$. For the latter, they are higher since the foil experiences higher net light pressure. For $\Delta\varphi = \pi$, both T_e and γ_e remain almost unchanged in the range $5 < a_0 < 20$, since $f_p = 0$ and the foil remains symmetrically compressed. With larger a_0 the foil becomes more relativistically transparent and its axial distortion becomes more pronounced, resulting in significantly larger T_e and γ_e. Figures 7(d)–7(f) show the dependence of k_m and γ_m on a_0 for different $\Delta\varphi$ values. Since for $\Delta\varphi = \pi$, E_r should be less than E_0 but not null (as the foil is not fully transparent), we set $E_r = E_0/2$ in the corresponding theory. We can see that for larger a_0, k_m and γ_m first decrease and increase (rising stage, blue shaded) with a_0, respectively, and then become nearly level (saturation stage, orange shaded). For $a_0 \leq 20$, the behaviour agrees well with that given by Equations (6) and (7) for the RTI. For the $\Delta\varphi = \pi$ case, γ_m is smallest and E_r is near null. Figures 7(d)–7(f) show that for less phase-matched laser pairs, the threshold light intensity is larger and the growth rate is smaller, suggesting that the instability can be manipulated by tailoring the phases of the paired lasers.

Several theoretical models have been proposed to explain the RTI. We have used Wan *et al.*'s model[17] since there the effect of electron temperature is included, which can be important in the problem here. It is also helpful for identifying which RTI and/or electron coupling effect governs the development of transverse foil instability.

6. Discussion

Although the simulations are for $d_0 = 0.1\lambda_0$, that is, comparable with that used in most related studies[18–22,25,27], our model is still applicable as long as the RIT condition $d_0 < d_m = 2a_0\omega_0 c/\omega_{pe}^2$ is satisfied. To illustrate the effect of d_0

on the laser–foil interaction, it is convenient to introduce the relativistic transparency factor $\eta = d_m/d_0$. Figure 8 shows the dependence of η, x_d, γ_m and k_m on d_0 for the LCP + RCP case with $\Delta\varphi = \pi/2$ from PIC simulations. One can see that for $d_0 < d_m$ and $\eta > 1$, the foil is transparent (grey shaded region). Both x_d and γ_m are relatively large and remain constant. As d_0 is increased ($d_0 > d_m$, $\eta < 1$), k_m becomes larger and is different in the blue and orange shaded regions. The interaction first experiences the quasi-transparent (blue shaded) stage because RIT also occurs at a later time as the two lasers compress the foil and transverse instability develops, and x_d and γ_m decrease. If the foil is thicker (i.e., d_0 is larger, orange shaded region), the foil becomes opaque to the lasers and x_d rapidly decreases to 0, that is, the foil is not axially displaced. The instability growth rate γ_m also decreases to its minimum value.

It may be of interest to note that the foil density $50n_c$ used in our simulations is close to that of the cryogenic hydrogen jet in the laser-ion acceleration experiments[30]. Although use of microneedles behind the nozzle can further reduce the size of the jet[31], it is still difficult to experimentally produce ultrafine plasma jet with sub-micrometre thickness. With thicker and denser (such as solid-density hydrogen) foil, in order to obtain similar results as considered here, the laser intensity must be increased to satisfy the RIT condition.

In experiments, the spatiotemporal synchronization of two relativistic fs lasers can be difficult to implement. Recently, it has been shown that two relativistic fs laser pulses of the same polarization can be obtained by splitting a source laser pulse, and their properties precisely controlled to within the micrometre and femtosecond scale[32]. Two laser pulses with different polarizations should thus be realizable with a plasma-based waveplate[33], and the time delay caused by the waveplate can be rectified by a suitable compensation plate.
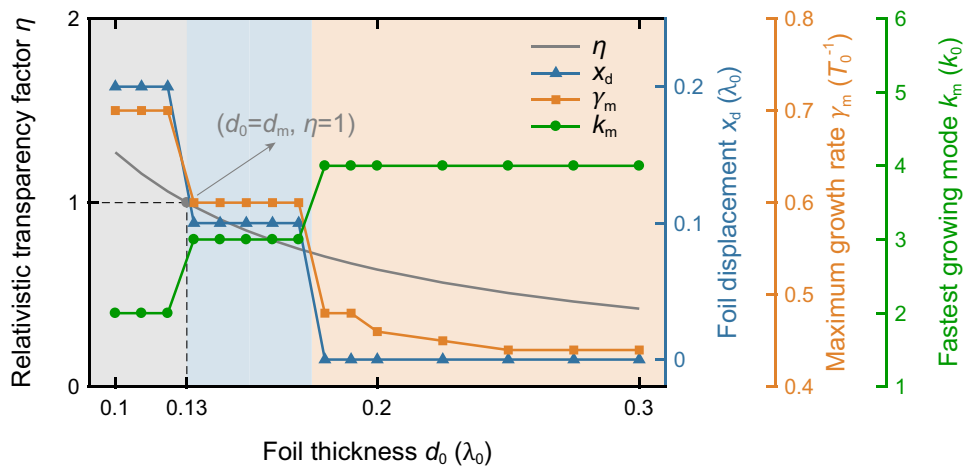

Figure 8. Relativistic transparency factor η (grey curve), displacement of the foil centre x_d (blue triangles), maximum growth rate γ_m (orange squares) and fastest growing mode k_m (green dots) versus the foil thickness d_0 from PIC simulations for the LCP + RCP case with $\Delta\varphi = \pi/2$. For $a_0 = 20$ and $n_e = 50n_c$, the critical foil thickness for relativistic transparency to occur is $d_m = 0.13\lambda_0$.

7. Summary

To summarize, we have investigated the dynamics of two counter-propagating relativistic fs laser pulses interacting with ultrathin foil. It is found that the transverse feature of the foil depends on the polarization direction and intensity distribution of the resultant laser field, and its longitudinal motion is determined by the impulse of the longitudinal light pressure force of the resultant laser light. For the LCP + RCP case, a grainy bubble and ring structure, characteristic of thin-foil RTI, appears in the foil density. The maximum growth rate of the instability increases with the resultant laser intensity, first rapidly and then slowly. When the two lasers are out of phase, the instability is weakest. Our results should be helpful for understanding counter-propagating laser pair interaction with ultrathin foils, which has been proposed for the production of ultra-bright γ-rays[22,23], electron–positron pairs[34–37], pulsed neutrons[24–27], ultra-intense light[18], etc.

Acknowledgements

References

1. L. Rayleigh, Proc. London Math. Soc. **14**, 170 (1883).
2. G. I. Taylor, Proc. Royal Soc. London **201**, 192 (1950).
3. S. E. Bodner, M. H. Emery, and J. H. Gardner, Plasma Phys. Controll. Fusion **29**, 1333 (1987).
4. D. S. Clark, C. R. Weber, J. L. Milovich, J. D. Salmonson, A. L. Kritcher, S. W. Haan, B. A. Hammel, D. E. Hinkel, O. A. Hurricane, O. S. Jones, M. M. Marinak, P. K. Patel, H. F. Robey, S. M. Sepke, and M. J. Edwards, Phys. Plasmas **23**, 056302 (2016).
5. A. B. Zylstra, O. A. Hurricane, D. A. Callahan, A. L. Kritcher, J. E. Ralph, H. F. Robey, J. S. Ross, C. V. Young, K. L. Baker, D. T. Casey, *et al.*, Nature **601**, 542 (2022).
6. T. Esirkepov, M. Borghesi, S.V. Bulanov, G. Mourou, and T. Tajima, Phys. Rev. Lett. **92**, 175003 (2004).
7. E. Ott, Phys. Rev. Lett. **29**, 1429 (1972).
8. F. Pegoraro and S. V. Bulanov, Phys. Rev. Lett. **99**, 065002 (2007).
9. T. P. Yu, A. Pukhov, G. Shvets, and M. Chen, Phys. Rev. Lett. **105**, 065002 (2010).
10. A. Sgattoni, S. Sinigardi, L. Fedeli, F. Pegoraro, and A. Macchi, Phys. Rev. E **91**, 013106 (2015).
11. C. A. J. Palmer, J. Schreiber, S. R. Nagel, N. P. Dover, C. Bellei, F. N. Beg, S. Bott, R. J. Clarke, A. E. Dangor, S. M. Hassan, P. Hilz, D. Jung, S. Kneip, S. P. D. Mangles, K. L. Lancaster, A. Rehman, A. P. L. Robinson, C. Spindloe, J. Szerypo, M. Tatarakis, M. Yeung, M. Zepf, and Z. Najmudin, Phys. Rev. Lett. **108**, 225002 (2012).
12. D. Wu, C. Y. Zheng, B. Qiao, C. T. Zhou, X. Q. Yan, M. Y. Yu, and X. T. He, Phys. Rev. E **90**, 023101 (2014).
13. M. L. Zhou, J. H. Bin, D. Haffa, X. Q. Yan, and J. Schreiber, Plasma Phys. Control. Fusion **59**, 055020 (2017).
14. H.-G. J. Chou, A. Grassi, S. H. Glenzer, and F. Fiuza, Phys. Rev. Res. **4**, L022056 (2022).
15. H.-G. J. Chou, A. Grassi, S. H. Glenzer, and F. Fiuza, J. Plasma Phys. **88**, 905880606 (2022).
16. X. Q. Yan, M. Chen, Z. M. Sheng, and J. E. Chen, Phys. Plasmas **16**, 044501 (2009).
17. Y. Wan, I. A. Andriyash, W. Lu, W. B. Mori, and V. Malka, Phys. Rev. Lett. **125**, 104801 (2020).
18. B. F. Shen and M. Y. Yu, Phys. Rev. Lett. **89**, 275004 (2002).
19. W. M. Zhang and M. Y. Yu, Appl. Phys. Lett. **99**, 141501 (2011).
20. M. Kumar, H. S. Song, J. Lee, D. Park, H. Suk, and M. S. Hur, Sci. Rep. **13**, 4233 (2023).
21. B. F. Shen and J. Meyer-ter-Vehn, Phys. Plasmas **8**, 1003 (2001).
22. B. F. Shen and J. Meyer-ter-Vehn, Phys. Rev. E **65**, 016405 (2001).
23. W. Luo, Y. B. Zhu, H. B. Zhuo, Y. Y. Ma, Y. M. Song, Z. C. Zhu, X. D. Wang, X. H. Li, I. C. E. Turcu, and M. Chen, Phys. Plasmas **22**, 063112 (2015).
24. A. Macchi, Appl. Phys. B **82**, 337 (2006).
25. X. M. Zhang, B. F. Shen, Z. B. Fang, and M. Y. Yu, J. Plasma Phys. **72**, 635 (2006).
26. L. X. Hu, T. P. Yu, F. Q. Shao, Q. J. Zhu, Y. Yin, and Y. Y. Ma, Phys. Plasmas **22**, 123104 (2015).
27. K. Y. Feng, F. Q. Shao, X. R. Jiang, D. B. Zou, L. X. Hu, G. B. Zhang, X. H. Yang, Y. Yin, Y. Y. Ma, and T. P. Yu, Acta Phys. Sin. **72**, 185201 (2023).
28. T. D. Arber, K. Bennett, C. S. Brady, A. Lawrence-Douglas, M. G. Ramsay, N. J. Sircombe, P. Gillies, R. G. Evans, H. Schmitz, A. R. Bell, and C. P. Ridgers, Plasma Phys. Control. Fusion **57**, 113001 (2015).
29. V. A. Vshivkov, N. M. Naumova, F. Pegoraro, and S. V. Bulanov, Phys. Plasmas **5**, 2727 (1998).
30. M. Gauthier, J. B. Kim, C. B. Curry, B. Aurand, E. J. Gamboa, S. Göde, C. Goyon, A. Hazi, S. Kerr, A. Pak, A. Propp, B. Ramakrishna, J. Ruby, O. Willi, G. J. Williams, C. Rödel, and S. H. Glenzer, Rev. Sci. Instrum. **87**, 11D827 (2016).
31. H. L. Guo, J. Q. Liu, X. Chen, B. Yang, and C. S. Yang, High Power Laser Particle Beams **27**, 024114 (2015).
32. Q. Chen, D. Maslarova, J. Z. Wang, S. X. Lee, V. Horný, and D. Umstadter, Phys. Rev. Lett. **128**, 164801 (2022).
33. G. Lehmann and K. H. Spatschek, Phys. Rev. E **97**, 063201 (2018).
34. A. R. Bell and J. G. Kirk, Phys. Rev. Lett. **101**, 200403 (2008).
35. E. N. Nerush, I. Yu. Kostyukov, A. M. Fedotov, N. B. Narozhny, N. V. Elkina, and H. Ruhl, Phys. Rev. Lett. **106**, 035001 (2011).
36. S. S. Bulanov, C. B. Schroeder, E. Esarey, and W. P. Leemans, Phys. Rev. A **87**, 062110 (2013).
37. M. Lobet, C. Ruyer, A. Debayle, E. d'Humières, M. Grech, M. Lemoine, and L. Gremillet, Phys. Rev. Lett. **115**, 215003 (2015).